Chinese Physics Letters

EXPRESS LETTER

Inelastic Dark Matter and High-Energy Recoil Signatures in LZ

Cite as: Zi-Tong Fan *et al*. 2026 *Chin. Phys. Lett.* **43** 110201

DOI CSTR

Recommended Articles

Ultralight Scalar and Axion Dark Matter Detection with Long-Baseline Atom Interferometers
Wei Zhao, Hui Liu, and Xitong Mei
Chin. Phys. Lett. **41**, 129501 (2024)

XTE J1814-338 as a Strange Star Admixed with Bosonic Dark Matter
Shuhua Yang, and Fridolin Weber
Chin. Phys. Lett. **43**, 021102 (2026)

Primordial Black Holes Formed during Magneto-Hydrodynamic Turbulence in the Early Universe as Dominant Part of Dark Matter
Jia-Xiang Liang, Peng Xu, Ming-Hui Du, and Zi-Ren Luo
Chin. Phys. Lett. **42**, 111101 (2025)

Search for Ultralight Dark Matter with a Frequency Adjustable Diamagnetic Levitated Sensor
Rui Li, Shaochun Lin, Liang Zhang, Changkui Duan, Pu Huang, and Jiangfeng Du
Chin. Phys. Lett. **40**, (2023)

A series journal of Chinese Physical Society distributed by IOP Publishing

Chinese Physics Letters

Chin. Phys. Lett. **43** 110201 (2026)

EXPRESS LETTER

DOI: 10.1088/0256-307X/43/11/110201
CSTR: 32039.14.0256-307X.43.11.110201

Inelastic Dark Matter and High-Energy Recoil Signatures in LZ

Zi-Tong Fan[1], Hong-Jian He[1,2,3,*], Yu-Chen Wang[1,*], and Yue Zhao[4,*]

[1]State Key Laboratory of Dark Matter Physics, Tsung-Dao Lee Institute & School of Physics and Astronomy, Shanghai Jiao Tong University, Shanghai 201210, China
[2]Department of Physics, Tsinghua University, Beijing 100084, China
[3]Center for High Energy Physics, Peking University, Beijing 100871, China
[4]Department of Physics and Jockey Club Institute for Advanced Study, The Hong Kong University of Science and Technology, Hong Kong, China

[*]Corresponding authors. Email: hjhe@sjtu.edu.cn; wang-yc15@tsinghua.org.cn; zhaoyue.hep@gmail.com

We study the inelastic dark matter (iDM) that consists of two-component dark matter (DM) particles (χ_1, χ_2) and serves as a minimal extension beyond the commonly used one-component DM models. A distinctive feature of such iDM scattering with the target nuclei is to favorably produce signals at high nuclear recoil energy region in both exothermic and endothermic processes. In particular, for the exothermic DM scenario, the signal does not rely on the tail of the Boltzmann velocity distribution. As a result, the required DM–nucleus scattering cross section is significantly reduced, which in turn helps to substantially relax the stringent constraints imposed by IceCube neutrino searches. Using the iDM–nucleus scattering, we naturally explain the newly reported event excess at high recoil energy with the LUX-ZEPLIN (LZ) experiment.

Introduction

Identifying the particle nature of dark matter (DM) poses a central challenge in particle physics and cosmology. Direct DM detection provides a fundamental means to overcome this challenge by searching for the energy deposited when Galactic DM scatters on ordinary matter. A confirmed signal would establish a nongravitational interaction of DM and offer information about its mass and couplings. This prospect has motivated extensive experimental efforts so far, including LUX-ZEPLIN (LZ) [1], XENON1T [2], and PandaX [3], which have placed stringent constraints on DM–nucleon scattering.

For conventional weakly interacting massive particles (WIMPs), these searches primarily target low-energy nuclear recoils (NRs). In the standard picture of momentum-independent, elastic scattering, the recoil energy is supplied entirely by the kinetic energy of nonrelativistic halo particles. Larger recoils require faster incident particles, while the nuclear form factor further suppresses scattering at large momentum transfer. The resulting spectrum is thus concentrated at low energies and falls rapidly toward higher energies.

The recent LZ observation [4] presents an unusual departure from this expectation. In a search extending the NR energy window to approximately 270 keV, the collaboration reported one event consistent with a NR of $E_{\rm R} = 248 \pm 23\,({\rm stat}) \pm 23\,({\rm sys})$ keV in a region with a low expected background [4]. The analysis finds a local significance of 3.4σ across the tested models and a global significance of 2.6σ. The challenge for a conventional WIMP interpretation is not simply the large recoil energy, but its occurrence without a corresponding low-energy excess. Increasing the elastic scattering cross section to account for the high-energy event would simultaneously enhance the more abundant low-energy recoils. Hence, a DM explanation calls for a mechanism that can properly change the shape of the recoil spectrum, instead of merely its normalization.

Inelastic scattering [5] offers such a mechanism and has motivated several interpretations of the LZ event [6–46], whereas other types of interpretations have been discussed [47–52]. An inelastic process can be either endothermic or exothermic. In an endothermic process, an incident DM particle scatters into a heavier state. The excitation energy introduces a kinematic threshold that suppresses low-energy recoils and can shift the signal toward the observed energy. However, many well-motivated realizations of such a model, like Higgsino in supersymmetry, are subject to stringent constraints from searches for high-energy neutrinos from the Sun [53]. The large cross section in the endothermic scenarios predicts large neutrino flux from DM annihilation inside the Sun. Thus, the absence of the corresponding IceCube signal [54] excludes the thermal Higgsino interpretation of the LZ event.

On the other hand, the exothermic inelastic scattering [55–59] also presents high-energy recoils by injecting the energy from the mass splitting into the final-state kinetic energy and produces signals compatible with the LZ event [19–21]. For suitable masses and splittings, this process generates a characteristic recoil scale at high energy and kinematically suppresses the recoils near the zero energy. Hence, it can produce the spectral pattern indicated by the LZ anomaly without relying solely on the high-speed tail of the halo. Particularly, for the same DM mass, mass splitting (with opposite signs), and cross section, the exothermic process always induces a stronger signal than the endothermic process due to kinematic enhancement. This requires lower interaction strength to explain the LZ data, and so it is easier to evade other constraints. Exothermic kinematics, together with a sufficiently suppressed solar neutrino yield, thus offers a route to addressing both the recoil spectrum problem and the indirect detection tension.

In this work, we investigate both exothermic and endothermic inelastic dark matter (iDM) as an attractive interpretation to the observed event excess in the LZ experiment. In the next section, we study the inelastic scattering mechanism in a minimal two-state setup with a short-range, spin-independent interaction and calculate the expected NR event rate in LZ. We examine its compatibility with the LZ candidate in the following section. We also discuss the requirements for a surviving excited state population and the conditions under which solar neutrino constraints can be avoided in the subsequent section. Finally, we conclude in the last section.

Received 15 September 2026; accepted 1 October 2026; published 4 November 2026

© 2026 Chinese Physical Society and IOP Publishing Ltd. All rights, including for text and data mining, AI training, and similar technologies, are reserved.

Check for updates

Theoretical Setup for iDM

In this section, we first set up the minimal iDM and discuss its kinematic properties. Then, we present the effective iDM–nucleon interaction and calculate the inelastic NR rates.

Minimal iDM

We consider two nearly degenerate Dirac fermions, χ_1 and χ_2, with a common mass scale $m_\chi \simeq m_{\chi_1} \simeq m_{\chi_2}$. For the transition $\chi_1 + N \to \chi_2 + N$, we define the DM mass splitting,

$$\Delta m = m_{\chi_1} - m_{\chi_2}. \tag{1}$$

Thus, the case of $\Delta m > 0$ denotes the exothermic scattering, whereas the case of $\Delta m < 0$ corresponds to the endothermic scattering. In either case, χ_1 always labels the incident state.

We denote the target nuclear mass by m_N and $\mu_N = m_\chi m_N/(m_\chi + m_N)$ is the reduced mass. The energy and momentum conservations in the center-of-mass frame give the following conditions:

$$\frac{1}{2}\mu_N v^2 + \Delta m = \frac{1}{2}\mu_N v'^2, \quad \boldsymbol{q} = \mu_N(\boldsymbol{v} - \boldsymbol{v}'), \tag{2}$$

where $\boldsymbol{v}$ and $\boldsymbol{v}'$ are the relative velocities of the initial and final states respectively. The NR energy is $E_\mathrm{R} = q^2/(2m_N)$. Then, the minimal relative velocity kinematically allowed is given by

$$v_\mathrm{min}(E_\mathrm{R}) = \frac{1}{\sqrt{2m_N E_\mathrm{R}}}\left|\frac{m_N E_\mathrm{R}}{\mu_N} - \Delta m\right|. \tag{3}$$

For exothermic scattering, v_min vanishes when the NR energy $E_\mathrm{R} = \mu_N \Delta m/m_N$, where an enhancement of signal is expected. Also, for any nonzero Δm, $v_\mathrm{min} \sim \Delta m/\sqrt{2m_N E_\mathrm{R}}$ diverges as $E_\mathrm{R} \to 0$. This suppresses low NR events and makes the exothermic process relevant to the LZ event.

For endothermic scattering, the minimum of $v_\mathrm{min}(E_\mathrm{R})$ occurs at $E_\mathrm{R} = \mu_N|\Delta m|/m_N$ and this minimum equals $\sqrt{2|\Delta m|/\mu_N}$. The energy conservation (2) imposes an upper bound on the DM mass splitting in the case,

$$|\Delta m| < \frac{1}{2}\mu_N v_\mathrm{max}^2. \tag{4}$$

At recoil energy around $E_\mathrm{R} = \mu_N \Delta m/m_N$, we always have the following inequalities for the minimal relative incident velocities in the exothermic, elastic, and endothermic scattering cases:

$$v_\mathrm{min}^\mathrm{exo} < v_\mathrm{min}^\mathrm{elastic} < v_\mathrm{min}^\mathrm{endo}. \tag{5}$$

Hence, for producing the same event rate, the exothermic scattering requires the weakest interaction strength, whereas the endothermic scattering requires the strongest.

Interaction and NR Spectrum

We formulate the spin-independent iDM–nucleon interaction by an off-diagonal vector-type effective Lagrangian,

$$\mathcal{L}_\mathrm{eff} = \frac{1}{\Lambda^2}\sum_{a=p,n} c_a(\bar{\chi}_2\gamma^\mu\chi_1)(\bar{a}\gamma_\mu a) + \mathrm{h.c.} \tag{6}$$

χ_1 and χ_2 can also represent four-component Majorana fermions, in which case the coefficients c_a are purely imaginary. We note that the diagonal terms can be absent and thus tree-level elastic scattering vanishes, as shown by the UV-completion theories in the literature [57,58].

We define the reference iDM–proton scattering cross section and the corresponding nuclear normalization as follows:

$$\sigma_p = \frac{\mu_p^2|c_p|^2}{\pi\Lambda^4}, \tag{7a}$$

$$\sigma_N^0 = \sigma_p\frac{\mu_N^2}{\mu_p^2}\left|Z + (A-Z)\frac{c_n}{c_p}\right|^2, \tag{7b}$$

where A and Z denote the atomic mass and charge respectively. We consider the conventional isospin symmetry between proton and neutron, which gives $c_n = c_p$ and the familiar coherent factor A^2 in Eq. [7(b)]. The differential recoil cross section is given by

$$\frac{\mathrm{d}\sigma_N}{\mathrm{d}E_\mathrm{R}} = \frac{m_N\sigma_N^0}{2\mu_N^2 v^2}F^2(q), \tag{8}$$

where the nuclear response is modeled with the Helm form factor,

$$F^2(q) = \left[\frac{3j_1(qr_N)}{qr_N}\right]^2 \mathrm{e}^{-(qs)^2}, \quad r_N = 1.14A^{1/3}\ \mathrm{fm}, \quad s = 0.9\ \mathrm{fm}. \tag{9}$$

The above formulas hold for the non-relativistic limit and the same formulas apply to the case of scalar iDM.

The typical momentum transfer is $q_0 \simeq 0.25$ GeV around the recoil energy 248 keV. For a mediator with a heavy mass $m_V^2 \gg q_0^2$, the propagator induces a factor of m_V^{-4}, relatively suppressing low-energy recoils as compared to the light-mediator case where the propagator contribution scales as $q^{-4} \propto E_\mathrm{R}^{-2}$.

Let ρ_in be the density of the incident DM particles. The differential rate per unit detector mass is given by

$$\frac{\mathrm{d}R}{\mathrm{d}E_\mathrm{R}} = \frac{\rho_\mathrm{in}}{m_\chi}\frac{\sigma_N^0}{2\mu_N^2}F^2(q)\eta(v_\mathrm{min}(E_\mathrm{R})), \tag{10}$$

with the function

$$\eta(v_\mathrm{min}) = \int_{v\geq v_\mathrm{min}} \mathrm{d}^3v\frac{f_\mathrm{gal}(\boldsymbol{v}+\boldsymbol{v}_e)}{v}. \tag{11}$$

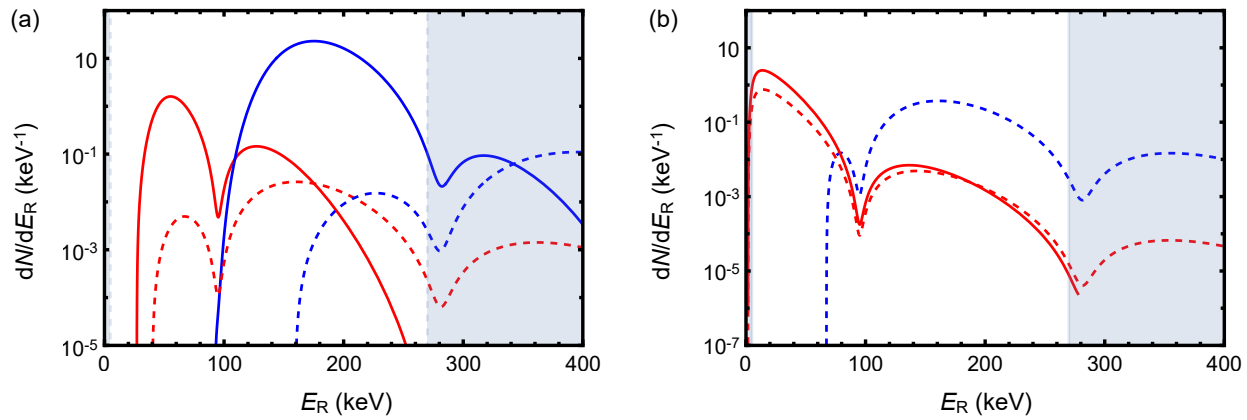

Fig. 1. (a) Spectra of true event number for the exothermic iDM. The solid (dashed) curves represent DM mass $m_\chi = 50$ GeV (500 GeV). The red curves are for $(\Delta m, \sigma_p) = (300\ \mathrm{keV}, 10^{-45}\ \mathrm{cm}^2)$, whereas the blue curves are for $(\Delta m, \sigma_p) = (700\ \mathrm{keV}, 10^{-43}\ \mathrm{cm}^2)$. (b) Spectra of true event number for the endothermic iDM. The solid (dashed) curves represent DM mass $m_\chi = 200$ GeV (900 GeV), The red curves are for $(\Delta m, \sigma_p) = (-50\ \mathrm{keV}, 10^{-45}\ \mathrm{cm}^2)$, whereas the blue curves are for $(\Delta m, \sigma_p) = (-250\ \mathrm{keV}, 10^{-41}\ \mathrm{cm}^2)$. The gray shaded regions at $E_\mathrm{R} < 5$ keV and $E_\mathrm{R} > 270$ keV indicate where the detection efficiency is below 50%. Note that there is no blue solid curve in panel (b), because it is kinematically forbidden.

The velocity distribution $f_{\rm gal}(\boldsymbol{v})$ is a Maxwell–Boltzmann distribution truncated at the escape velocity $v_{\rm esc}$ and normalized to unity. For illustration, we adopt the Standard Halo Model with inputs $\rho_{\rm DM} = 0.3$ GeV$\cdot$cm^{-3}, $v_0 = v_e = 0.00073c$, and $v_{\rm esc} = 0.00181c$, neglecting annual modulation [60]. Thus, $v_{\rm max} = v_{\rm esc} + v_e = 0.00254c$. Without loss of generality, we choose $\rho_{\rm in} = \rho_{\rm DM}$ henceforth.

We obtain the true event spectra by multiplying Eq. (10) with the exposure of the LZ experiment, $\mathcal{E} = 2.84$ tonne-years. In Fig. 1(a) we show the exothermic case where $\Delta m > 0$. It is clear that the larger m_χ and larger Δm give higher $E_{\rm R}$ thresholds, and are more compatible with the event excess at $E_{\rm R} \sim 248$ keV. However, the larger $(m_\chi, \Delta m)$ values also predict much more events in the higher NR region, and will be constrained by the higher-energy sideband (HE SB).* The endothermic iDM ($\Delta m < 0$) in Fig. 1(b) also shows that larger m_χ and larger $|\Delta m|$ give higher $E_{\rm R}$ thresholds. We note that there is no blue solid curve in Fig. 1(b). This is because it violates the condition (4).

Analyzing iDM Signatures for LZ

In this section, we study the iDM signal in LZ detectors and perform a simplified profile likelihood analysis to set limit for m_χ, Δm and σ_p.

Detector Response and Statistical Methods

We use the efficiency $\epsilon(E_{\rm R})$ digitized from Fig. S2 of Ref. [4] and the exposure $\mathcal{E} = 2.84$ tonne-years to calculate the event numbers:

$$\frac{{\rm d}N}{{\rm d}E_{\rm d}} = \mathcal{E}\int_0^\infty {\rm d}E_{\rm R} G(E_{\rm d}; E_{\rm R}, \sigma_{\rm E}(E_{\rm R}))\epsilon(E_{\rm R})\frac{{\rm d}R}{{\rm d}E_{\rm R}}, \tag{12}$$

where $E_{\rm d}$ is the detected energy, G a normalized Gaussian kernel and $\sigma_{\rm E}$ the energy resolution. The uncertainty can be estimated as $\sigma_{\rm E} = \sqrt{\sigma_{\rm stat}^2 + \sigma_{\rm sys}^2}$, with

$$\sigma_{\rm stat}(E_{\rm R}) = 1.46\sqrt{E_{\rm R}},\ \ \sigma_{\rm sys}(E_{\rm R}) = 0.093E_{\rm R}, \tag{13}$$

where all quantities are in the unit of keV.

We use the three intervals [70, 215.5], [215.5, 280.5], and [280.5, 305] keV for $E_{\rm d}$ binning and assign the event numbers $(n_1, n_2, n_3) = (0, 1, 0)$. For the lower bound of $E_{\rm d}$, we adopt from Fig. 2 of Ref. [4], $E_{\rm d}^{\rm min} = 70$ keV, above which the electron-recoil/NR discrimination becomes effective. The upper bound $E_{\rm d}^{\rm max} = 305$ keV is simply derived by 270 keV + $\sigma_{\rm E}$(270 keV), where the value 270 keV is the NR energy at which the efficiency falls below 50%. The total background count is only 0.0106 ± 0.0008 [4], and thus is neglected for simplicity in the following.

For fixed $(m_\chi, \Delta m)$ values, we write the expected signal counts as μs_i, where μ is the dimensionless parameter for the signal strength and s_i is the predicted event number in the i-th bin (for a benchmark σ_N). The background-free likelihood is given by

$$\mathcal{L}(\mu; m_\chi, \Delta m) = \mu s_2 {\rm e}^{-\mu s_{\rm tot}},\ \ s_{\rm tot} = \sum_{i=1}^{3} s_i. \tag{14}$$

This likelihood function can be maximized analytically with respect to μ. It gives the best fit value $\hat{\mu}$, and the corresponding profiled likelihood $\mathcal{L}_{\rm prof}$ for $(m_\chi, \Delta m)$:

$$\hat{\mu}(m_\chi, \Delta m) = \frac{1}{s_{\rm tot}},\ \ \mathcal{L}_{\rm prof}(m_\chi, \Delta m) = \frac{s_2}{s_{\rm tot}{\rm e}}. \tag{15}$$

Thus, the fitted total signal count is always one, and the fit quality affected by the spectral shape is represented solely by the fraction of the accepted signal in the event-containing interval.

For the shape comparison, we define the test statistic

$$\chi^2(m_\chi, \Delta m) = -2\ln(\mathcal{L}_{\rm prof}), \tag{16}$$

to perform the likelihood-based test for limit setting.

Analyzing iDM Signatures at High Recoil Energy

We scan over the parameter space of $10\ {\rm GeV} \leqq m_\chi \leqq 1000\ {\rm GeV}$ and $-500\ {\rm keV} \leqq \Delta m \leqq 1000\ {\rm keV}$, excluding kinematically inaccessible regions where the condition (4) is not satisfied. The upper bound for m_χ is to avoid excesses in the higher-energy sideband, and the upper bound for the mass splitting is simply $\Delta m < 2m_e$. The lower bounds for m_χ and Δm are for kinematic reasons.

Figure 2 shows the best fit results and 90% C.L. intervals for the DM–proton scattering cross section σ_p versus DM mass m_χ. (For simplicity, in converting the DM–nucleus scattering cross section σ_N to σ_p, we adopt the conventional assumption of isospin symmetry between proton and neutron.) In Fig. 2(a) for endothermic scattering, we see that each value of $|\Delta m|$ sets a cutoff on m_χ from below. This can be derived from the kinematic condition in Eq. (4), which implies

$$\mu_N v_{\rm max}^2 > 2|\Delta m|,\ \ m_\chi > \frac{2m_N|\Delta m|}{m_N v_{\rm max}^2 - 2|\Delta m|}. \tag{17}$$

The scan also contains a broad exothermic region with favorable spectral likelihood, as shown in Fig. 2(b). In both plots, the reduced masses and spectral shape approach constants for $m_\chi \gg m_N$, whereas the incident number density remains proportional to m_χ^{-1}. Comparing the results between Figs. 2(a) and 2(b), we see that the exothermic case in general requires much smaller cross section to fit the event. This is explained by Eq. (5).

We plot the best fit results and 90% C.L. intervals for the DM–nucleon scattering cross section σ_p versus the mass splitting Δm in

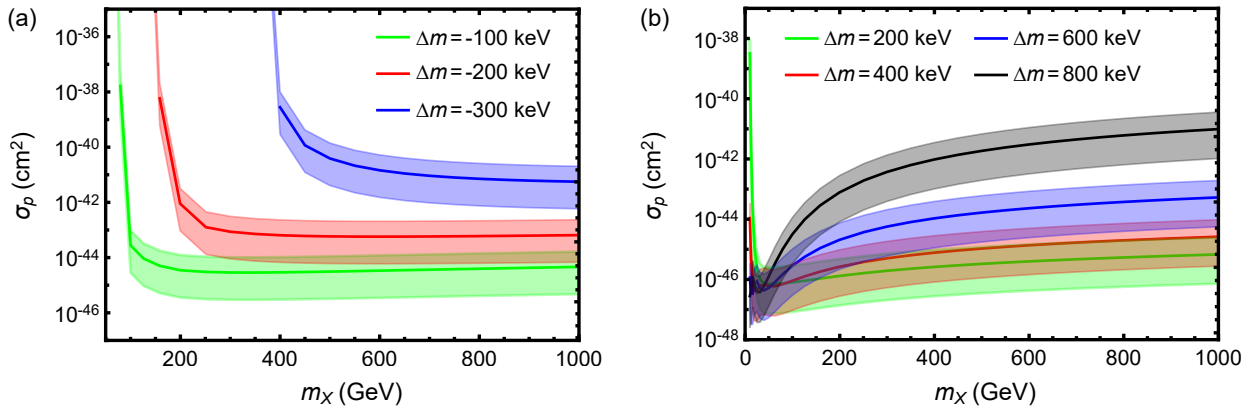

Fig. 2. Best fits (solid curves) and 90% C.L. intervals (shaded bands) on the DM–proton scattering cross section. (a) Limits on σ_p versus m_χ for endothermic iDM, with benchmark values of Δm as stated in the plot legend. (b) Limits on σ_p versus m_χ for exothermic iDM, with benchmark values of Δm as stated in the plot legend.

*Higher-energy sideband information is particularly important when the spectrum extends beyond the main acceptance. The potential importance of this test has also been emphasized in Refs. [17,19]. Without further information of the sideband, in this work we do not establish a sideband exclusion or an upper bound on the DM mass.

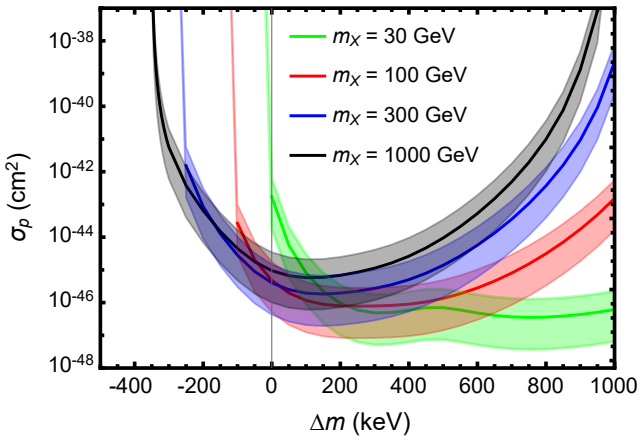

Fig. 3. Best fits (solid curves) and 90% C.L. intervals (shaded bands) on the DM–proton scattering cross section versus Δm for both endothermic and exothermic iDM. The benchmark values of m_χ as depicted in the plot legend.

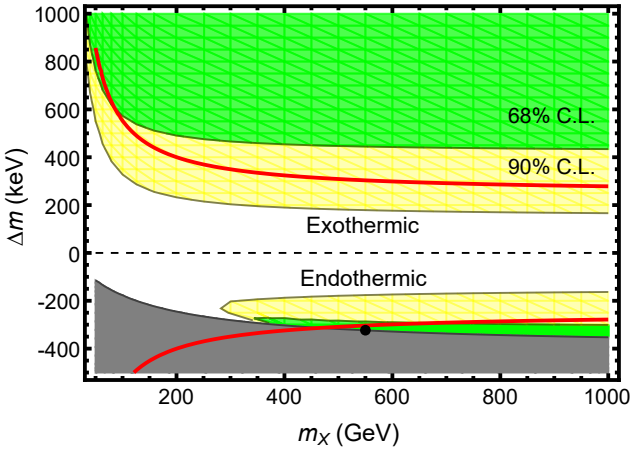

Fig. 4. Best fit value (black dot), 68% C.L. limits (green regions) and 90% C.L. limits (yellow regions) for the DM mass m_χ and mass splitting Δm. The gray shaded region is kinematically forbidden. The red curves represent the case where a peak at $E_R = 248$ keV is predicted.

Fig. 3. The left region with $\Delta m < 0$ stands for the endothermic scattering, whereas the right region with $\Delta m > 0$ is for the exothermic scattering. For each value of m_χ, there is a lower limit on Δm, which is exactly determined by Eq.(4).

In Fig. 4, we show the 68% C.L. and 90% C.L. contours on the $m_\chi - \Delta m$ plane. The red curves represent $|\Delta m| = (m_N/\mu_N) \times 248$ keV, in which case a peak at $E_R = 248$ keV is predicted. The gray shaded area is kinematically forbidden by violating the condition (4). The scan places its largest likelihood near $(m_\chi, \Delta m) \simeq (550\,\text{GeV}, -323\,\text{keV})$. The best fit point is understandable as a near-boundary solution rather than a well-determined iDM benchmark. At the boundary we have $|\Delta m| = \mu_N v_{\max}^2/2$. Setting $E_R = \mu_N |\Delta m|/m_N = 248$ keV gives $m_\chi \sim 466$ GeV and $|\Delta m| \sim 313$ keV, which explains the best fit values. This boundary point gives a narrow spectrum whose shape fits the excess very well, but its rate tends to zero. To fit the observed event using the boundary point requires a divergent cross section, thus this best-fit point is not physical. Similarly for the exothermic case, as discussed in above section, the larger $(m_\chi, \Delta m)$ values produce much more events in the higher NR energy region ($\gtrsim$300 keV), and the observed event at 248 keV corresponds to the low-energy tail of the full spectrum. Hence, a much larger total event number (and thus a much larger cross section) is expected to explain this event. Such large values of $(m_\chi, \Delta m)$ should be constrained once the HE SB data is released, and we expect that the red curve would become more favored by data. Despite these unphysical regions, the majority of the parameter space inside the 90% C.L. contours belongs to the exothermic case. We further note that at 68% C.L. the endothermic case favors $165\,\text{keV} < |\Delta m| < 350\,\text{keV}$, whereas the exothermic case favors $165\,\text{keV} < \Delta m < 1000\,\text{keV}$.

Cosmological and Astrophysical Constraints

In this section, we present the cosmological and astrophysical constraints on the iDM scenario. We first discuss the heavier-state abundance and its longevity. Then, we estimate the solar capture of the exothermic and endothermic iDM as well as study the total annihilation rates. We show that the iDM annihilation-induced solar neutrino signals are sufficiently suppressed and well below the IceCube neutrino bound.

Excited-State Abundance and Longevity

Conventionally, it is assumed that DM consists of only the lightest particle in the dark sector. However in the inelastic case, since there are two nearly degenerate states, the constituent of DM may differ and need to be revisited. From a purely theoretical standpoint, an endothermic process always requires a sufficient up-scattering cross section and a small enough mass splititng $\Delta m < m_\chi v^2 \sim 10^{-6} m_\chi$. Thus the two states must have been in thermal and chemical equilibrium in the early Universe and then freeze out with nearly equal abundances. If the heavier state is sufficiently long-lived, it should constitute a significant fraction of the local DM today. Consequently, the exothermic process is kinematically favored and could be the dominant contribution. Therefore, a proper treatment of the exothermic scattering is essential for a complete description of direct detection signals.

Throughout the analysis, we always study the endothermic and exothermic inelastic scatterings separately. This is because as long as the heavier component is as abundant as the lighter one, the exothermic process dominates because it is enhanced kinematically, as discussed by Eq. (5). From Fig. 2, we see that for $|\Delta m| = 200$ keV the endothermic case [the red curve in Fig. 2(a)] requires a cross section $(10^2$–$10^6)$ times larger than the exothermic case [the green curve in Fig. 2(b)]. Hence, to obtain comparable contributions from the endothermic and exothermic processes (having identical cross sections), it requires $\rho_\chi^{\text{heavy}}/\rho_\chi^{\text{light}} = 10^{-2}$–$10^{-6}$. For simplicity, we do not consider such a scenario in this work. Reference [21] has discussed the case of $\rho_\chi^{\text{heavy}}/\rho_\chi^{\text{light}} \sim 10^{-3}$, and showed that the exothermic process is still dominant. Hence, as long as the light and heavy DM particles coexist with comparable abundance, the main effect always comes from the heavier iDM component and we only need to take into account the exothermic scattering in direct detection experiments. This could be an additional reason to motivate the exothermic scenario.

However, comparable populations do not follow from near-degenerate masses alone. Firstly, a long decay lifetime is necessary for a primordial excited population. For the dark photon-mediated iDM model, the heavier state dominantly decays into the lighter state plus a neutrino-pair with the decay width [58]

$$\begin{aligned}\Gamma_{\chi_1 \to \chi_2 \nu\bar{\nu}} &\sim (4\times 10^{34}\ \text{yrs})^{-1} \left(\frac{\Lambda}{100\,\text{GeV}}\right)^{-4} \left(\frac{\Delta m}{10\,\text{keV}}\right)^{9} \\ &= (10^{25}\ \text{yrs})^{-1} \left(\frac{\Lambda}{\text{TeV}}\right)^{-4} \left(\frac{\Delta m}{300\,\text{keV}}\right)^{9},\end{aligned} \tag{18}$$

where Λ is the cutoff scale derived from the fitting. We see that the lifetime of the heavier state is substantially far beyond the age of the present Universe. Note that factors such as the fraction of the heavier state and the ratio between c_p and c_n will be taken into account for Λ; yet these factors do not change the conclusion. Secondly, other processes such as $\chi_1 + \chi_1 \leftrightarrow \chi_2 + \chi_2$ and $\chi_1 + e \leftrightarrow \chi_2 + e$ also deplete the abundance of the heavier state when the DM temperature T_χ falls below $|\Delta m|$. As long as these processes decouple at higher temperature

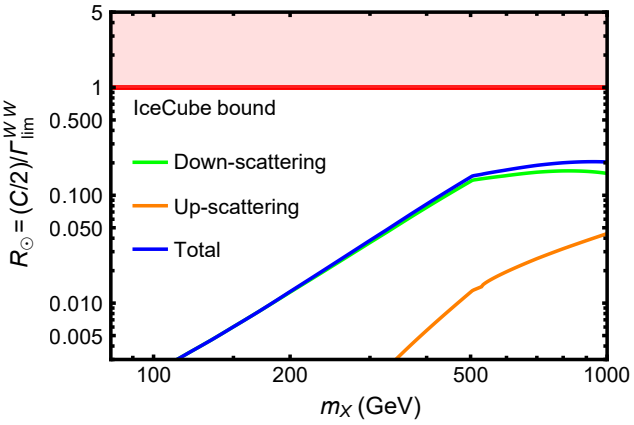

Fig. 5. The predicted exothermic iDM annihilation rate into W^+W^- relative to the IceCube bound [53,54], including heavier state down-scattering contribution (green line), lighter state up-scattering contribution (orange line), and total rate (blue line). Across the DM mass range under consideration, the exothermic iDM model readily evades the IceCube neutrino bound at 90% C.L. (red line). The mass splitting is derived from $\mu_N \Delta m/m_N = 248$ keV and the DM–nucleon cross section is fixed to the best fit of the LZ signal rate.

$T_\chi \gg |\Delta m|$, such depletion effects are negligible [56,57]. Since the thermal history is much more model-dependent than the lifetime, we would leave such detailed analyses to future work.

Solar Capture and IceCube Constraints

As discussed in the Introduction, the solar-neutrino problem of the inelastic Higgsino is unusually severe [53]. The LZ recoil is generated close to the endothermic kinematic boundary, so the terrestrial rate samples the extreme Galactic velocity tail, whereas solar acceleration to $w \gtrsim 1300\,\mathrm{km\cdot s^{-1}}$ removes much of this kinematic suppression. In addition, the Higgsino scattering strength is fixed by tree-level Z exchange and its dominant annihilation mode is W^+W^-, so both capture and the hard-neutrino yield are predictive.

Unlike the Higgsino scenario, solar-neutrino constraints are much weaker here. First, the exothermic DM scenario requires a significantly smaller scattering cross section with nucleus, since it does not rely on the velocity tail to reach the energy threshold. This drastically reduces the solar capture rate, such that even with dominant annihilation into electroweak bosons, IceCube imposes no constraint. Additionally, if annihilation does not predominantly produce electroweak bosons [26], the neutrino flux is further suppressed.[†] Thus, the exothermic parameter space considered here is essentially unconstrained by current solar-neutrino searches.

The kinematic distinction for exothermic and endothermic capture follows directly from energy conservation [61,62]. Firstly, the endothermic process requires the kinematic threshold given by Eq. (4). For light nuclei such as hydrogen and helium (which make up about 98% of the solar mass), the reduced mass is $\mu_N \approx m_N \approx O(\mathrm{GeV})$, thus the up-scattering is forbidden even with the maximal solar escape velocity $v_{\rm esc} \simeq 1380\ \mathrm{km/s} = 0.0046c$. Secondly, DM particle with asymptotic solar-frame speed u has speed w at radius r, obeying the relation

$$w^2 = u^2 + v^2_{\rm esc,\odot}(r). \tag{19}$$

Neglecting the thermal motion, an exothermic recoil leaves the DM with kinetic energy $\frac{1}{2}m_\chi w^2 + \Delta m - E_{\rm R}$ at the leading order in $\Delta m/m_\chi$. Requiring the outgoing state to remain gravitationally bounded thus gives

$$E_{\rm R} > \frac{1}{2}m_\chi u^2 + \Delta m. \tag{20}$$

Thus, although there is no kinematic threshold for the exothermic scattering, the extra energy from mass splitting makes it harder to capture the iDM. By contrast, endothermic up-scattering is subject to a kinematic threshold, but the excitation itself removes kinetic energy and gives $E_{\rm R} > \frac{1}{2}m_\chi u^2 - |\Delta m|$. Inside the Sun, the large local velocity w can partially alleviate the endothermic excitation threshold. Hence, the extra released energy in the exothermic case tends to suppress its capture rate.

We intentionally overestimate the solar neutrino signal as follows. We adopt, for all DM, a low mono-speed $u_0 = 200\,\mathrm{km\cdot s^{-1}}$ that favors capture, and assume a one-zone core model for the solar composition with the core potential $v_{\rm esc,\odot} = 1380\,\mathrm{km\cdot s^{-1}}$. Using the formulas $E^\pm_{\rm R}(w) = (\mu_N^2/2m_N)(w \pm \sqrt{w^2 + 2\Delta m/\mu_N})^2$ and $w_0^2 = u_0^2 + v^2_{\rm esc,\odot}$, we estimate the excited-state capture rate as

$$C_{\rm H} \simeq \frac{\rho_{\rm DM}}{m_\chi}\frac{w_0^2}{u_0} f_{\rm H}\sigma_p \sum_i N_i \frac{m_N A_i^2}{2\mu_p^2 w_0^2}\int_{E^{\rm cap}_{\rm R}}^{E^+_{\rm R}} \mathrm{d}E_{\rm R}\, F_i^2(q), \tag{21}$$

where $f_{\rm H}$ is the excited-state fraction, i denotes the species of the target nucleus, A_i the nuclear mass number, N_i the number of target nuclei in the Sun, $F_i(q)$ is the Helm form factor, and we have $E^{\rm cap}_{\rm R} = \max(E^-_{\rm R}, \Delta m + \frac{1}{2}m_\chi u_0^2)$. We note that the cross section σ_p is already strongly constrained by the LZ data, as discussed in the "Analyzing iDM" section. Given the inevitable presence of ground-state DM, we also estimate its solar capture rate by replacing Δm with $-\Delta m$ and the excited-state fraction $f_{\rm H}$ with the ground-state fraction $f_{\rm L}$ in Eq. (21). Following the discussion in the above section, we assume that the ground and excited states are equally abundant, $f_{\rm L}/f_{\rm H} = 1$. Thus, the total solar capture rate is given by $C = C_{\rm H} + C_{\rm L}$.

Then, we further make two assumptions that maximize the observable neutrino signal: the perfect capture-annihilation equilibrium, $\Gamma_{\rm ann} = C/2$, and the 100% annihilation branching fraction into W^+W^-. For this, we define a ratio,

$$\mathcal{R}_\odot = \frac{C/2}{\Gamma^{WW}_{\rm lim}(m_\chi)}, \tag{22}$$

where $\Gamma^{WW}_{\rm lim}$ is the iDM annihilation rate into W^+W^- as constrained by the IceCube solar neutrino flux [53], which is a function of m_χ. In Fig. 5, we plot $\mathcal{R}_\odot$ as a function of iDM mass. We choose $\mu_N\Delta m/m_N \sim 248$ keV for Δm, and set the DM–nucleon scattering cross section to be the best fit of the LZ event excess. As can be seen, the contribution of the heavier state is dominant, and the lighter state gives only subleading contribution in the higher-mass region.

In the LZ-relevant region, the total contribution from both lighter and heavier states remains comfortably below the IceCube-equivalent exclusion bound at 90% C.L. (the red line) even under all the above overestimates of solar neutrino signals. Hence, as is clear, already at the level of the initial capture rate, the LZ-compatible exothermic case predicts much less solar neutrino signals than the near-threshold endothermic case (such as Higgsino models), due to the smaller cross section in the exothermic case required by fitting the LZ data. Hence, a broad exothermic parameter space remains viable even under the assumptions deliberately chosen to overestimate the neutrino signals for the IceCube detection.

Conclusions

The iDM scattering produces a characteristic NR energy that differs from the elastic case. For both the exothermic and endothermic iDM cases, the incident speed required for a low-energy recoil diverges. This feature permits high-energy NR events without the low-energy spectral concentration of conventional elastic, spin-independent WIMP scattering. Mass splittings of several hundred keV are relevant to the LZ candidate event for weak-scale and heavier DM particle.

[†]Reference [21] considers the evasion solely due to the annihilation final state. But for exothermic iDM, the much smaller cross section lowers the solar capture rate enough to ensure a safe neutrino flux regardless of annihilation channels, as shown in Fig. 5.

In this work, we performed a model-independent study for both the exothermic and endothermic iDM and their NR signals in the LZ experiment. We analyzed the kinematics of the inelastic DM scattering and computed the corresponding NR spectra, showing that the high-energy NR event excess can be naturally explained by the iDM. We scanned over the iDM parameter space of $10\,\text{GeV} \leqq m_\chi \leqq 1000\,\text{GeV}$ and $-500\,\text{keV} \leqq \Delta m \leqq 1000\,\text{keV}$, and derived the best fits and 90% C.L. intervals on the DM–proton cross section as shown in Figs. 2 and 3. We further derived the bounds in the $(m_\chi, \Delta m)$ plane at 68% C.L. and 90% C.L. as presented in Fig. 4. Our results show that the LZ event favors the DM mass-splitting ranges within $165\,\text{keV} < |\Delta m| < 350\,\text{keV}$ for the endothermic iDM and within $165\,\text{keV} < \Delta m < 1000\,\text{keV}$ for the exothermic iDM. Also, the exothermic case can account for the LZ data with much smaller DM–nucleon cross sections. The abundance, longevity, and solar capture effects of exothermic iDM were discussed. We demonstrated that it is feasible for the heavier iDM state to be stable at the cosmological time scale, and the neutrino flux from the annihilation of solar captured exothermic iDM is well below the IceCube limits because of the much smaller DM–nucleon cross sections.

Acknowledgments

The works of ZTF, HJH and YCW were supported in part by the National Natural Science Foundation of China (NSFC) (Grant Nos. 12435005 and 12175136), the Shenzhen Science and Technology Program (Grant No. JCYJ20240813150911015), the State Key Laboratory of Dark Matter Physics, the Key Laboratory for Particle Astrophysics and Cosmology (MOE), and the Shanghai Key Laboratory for Particle Physics and Cosmology.

References

[1] Aalbers J, Akerib D S, Al Musalhi A K *et al*. (LZ Collaboration) 2025 *Phys. Rev. Lett.* **135** 011802
[2] Aprile E, Abe K, Agostini F *et al*. (XENON Collaboration) 2024 *Phys. Rev. D* **109** 112017
[3] Bo Z, Chen W, Chen X *et al*. (PandaX Collaboration) 2025 *Phys. Rev. Lett.* **134** 011805
[4] Akerib D S, Al Musalhi A K, Almquist B J *et al*. (LZ Collaboration) 2026 arXiv:2609.02823 [hep-ex]
[5] Tucker-Smith D and Weiner N 2001 *Phys. Rev. D* **64** 043502
[6] Su L, Yang J M, and Yang W N 2026 arXiv:2609.01475 [hep-ph]
[7] Fan J and Reece M 2026 arXiv:2609.01504 [hep-ph]
[8] Freese K and Theodosopoulos D P 2026 arXiv:2609.01583 [hep-ph]
[9] Wu L, Zhang Y, and Zhu B 2026 arXiv:2609.01590 [hep-ph]
[10] Lou Y and Lu C T 2026 arXiv:2609.01592 [hep-ph]
[11] Nomura Y 2026 arXiv:2609.02505 [hep-ph]
[12] Di Mauro M 2026 arXiv:2609.02608 [hep-ph]
[13] Visinelli L 2026 arXiv:2609.02807 [hep-ph]
[14] Yamashita K 2026 arXiv:2609.02868 [hep-ph]
[15] Smirnov J, Griffith S, and Beacom J F 2026 arXiv:2609.04144 [hep-ph]
[16] Du X and Wang F 2026 arXiv:2609.04163 [hep-ph]
[17] Rodd N L, Safdi B R, Slatyer T R, and Xu W L 2026 arXiv:2609.04175 [hep-ph]
[18] McCabe C 2026 arXiv:2609.04181 [hep-ph]
[19] Dent J B and Newstead J L 2026 arXiv:2609.04673 [hep-ph]
[20] de Lima C H 2026 arXiv:2609.05204 [hep-ph]
[21] Baer H and Barger V 2026 arXiv:2609.06153 [hep-ph]
[22] Lee H M 2026 arXiv:2609.06171 [hep-ph]
[23] Wang L and Xiao Y 2026 arXiv:2609.06571 [hep-ph]
[24] Yang M, Wu Q F, Tsai Y L S, and Fan Y Z 2026 arXiv:2609.06640 [hep-ph]
[25] Kotlarski W, Kowalska K, and Sessolo E M 2026 arXiv:2609.06750 [hep-ph]
[26] Di Mauro M and Shaikh H 2026 arXiv:2609.06760 [hep-ph]
[27] Das P, Karmakar B, Mahapatra S, and Paul P K 2026 arXiv:2609.06825 [hep-ph]
[28] Alhazmi H, Kim D, Kong K, Park J C, and Shin S 2026 arXiv:2609.06890 [hep-ph]
[29] Okada N and Seto O 2026 arXiv:2609.06909 [hep-ph]
[30] Ahmed W and Leontaris G K 2026 arXiv:2609.07138 [hep-ph]
[31] Du X Y, Huang W, and Xie K 2026 arXiv:2609.07225 [hep-ph]
[32] Bandyopadhyay D, Borah D, and Borah P 2026 arXiv:2609.07451 [hep-ph]
[33] Kannike K, Raidal M, and Strumia A 2026 arXiv:2609.07742 [hep-ph]
[34] Borah D, Sahoo S K, Sahu N, and Sharma S 2026 arXiv:2609.07800 [hep-ph]
[35] Bose D, Saha A K, Das D J *et al*. 2026 arXiv:2609.07807 [hep-ph]
[36] Bisal S, Cao J, and Li F 2026 arXiv:2609.07811 [hep-ph]
[37] Cheung K, Kang S K, and Kumar R 2026 arXiv:2609.08712 [hep-ph]
[38] Yuan G W, Zhang B, Cao W Y, Feng L, and Yang R 2026 arXiv:2609.08893 [hep-ph]
[39] Zhu P, Garcia G D V, Wang X G, Thomas A W, and White M J 2026 arXiv:2609.09015 [hep-ph]
[40] Asadi P, Batz A, Fox P J, Homiller S D, and Kribs G D 2026 arXiv:2609.09107 [hep-ph]
[41] Lee V S H and Randall L 2026 arXiv:2609.09136 [hep-ph]
[42] Lee S J and Youn T 2026 arXiv:2609.09138 [hep-ph]
[43] Langho K 2026 arXiv:2609.09385 [hep-ph]
[44] Nguyen T T Q, Linden T, and Hooper D 2026 arXiv:2609.11833 [hep-ph]
[45] Lian J and Yang J M 2026 arXiv:2609.15742 [hep-ph]
[46] Lian J and Yang J M 2026 arXiv:2610.09753 [hep-ph]
[47] Jeesun S and Majumdar A 2026 arXiv:2609.04185 [hep-ph]
[48] Unwin J 2026 arXiv:2609.04186 [hep-ph]
[49] Gu G, Li L, Tang S, and Xu Y 2026 arXiv:2609.05291 [hep-ph]
[50] Liang J H, Liu Z, Tran V Q, and Xu Y 2026 arXiv:2609.06756 [hep-ph]
[51] Elahi F and Schwaller P 2026 arXiv:2609.08993 [hep-ph]
[52] Aghaie M and Strumia A 2026 arXiv:2609.09037 [hep-ph]
[53] Pospelov M and Ramani H 2026 arXiv:2609.02775 [hep-ph]
[54] Abbasi R, Ackermann M, Adams J *et al*. (IceCube Collaboration) 2025 arXiv:2507.08457 [hep-ex]
[55] Graham P W, Harnik R, Rajendran S, and Saraswat P 2010 *Phys. Rev. D* **82** 063512
[56] He H J, Wang Y C, and Zheng J 2021 *JCAP* **01** 042
[57] He H J, Wang Y C, and Zheng J 2021 *Phys. Rev. D* **104** 115033
[58] He H J, Wang Y C, and Zheng J 2024 *Phys. Dark Univ.* **46** 101670
[59] Wang Y C, Yun Y, He H J, and Meng Y 2025 arXiv:2508.13062 [hep-ph]
[60] McCabe C 2010 *Phys. Rev. D* **82** 023530
[61] Blennow M, Clementz S, and Herrero-Garcia J 2016 *JCAP* **04** 004
[62] Blennow M, Clementz S and Herrero-Garcia J 2016 *Eur. Phys. J. C* **78** 386 [Erratum: 2019 *Eur. Phys. J. C* **79** 407]